Foam aging under free drainage analysed using associated operando techniques

Julien Lamolinairie,[a] Benjamin Dollet,[b] Jean-Luc Bridot,[c] Pierre Bauduin,[d] Olivier Diat,[d] and Leonardo Chiappisi[a*]

September 14, 2022

Abstract

Liquid foams are multi-scale structures whose structural characterization requires the combination of very different techniques. This inherently complex task is made more difficult by the fact that foams are also intrinsically unstable systems and that their properties are highly dependent on the production protocol and sample container. To tackle these issues, a new device has been developed that enables the simultaneous time-resolved investigation of foams by small-angle neutron scattering (SANS), electrical conductivity, and bubbles imaging. This device allows the characterization of the foam and its aging from nanometer up to centimeter scale on a single experiment. A specific SANS model was developed to quantitatively adjust the scattering intensity from the dry foam. Structural features such as the liquid fraction, specific surface area of the Plateau borders and inter-bubble films, thin film thickness were deduced from this analysis and some of them compared with extracted from the other applied techniques. This approach has been applied to a surfactant-stabilized liquid foam under free drainage and the underlying foam destabilization mechanisms were discussed with unprecedented detail. For example, the information extracted from the image analysis and SANS data allow for the first time to determine the disjoining pressure vs thickness isotherm in a real, draining foam.

1 Introduction

Liquid foam structure and aging are influenced by several physical and chemical parameters, such as the type of gas[1,2], the surfactant used[3,4], the liquid fraction[5–7], the size of bubbles[8,9], the thickness of the inter-bubble film[10–12], the surface tension[13,14] and the interfacial elastic modulus[15,16]. Predicting the dominant factors to control the resulting foam properties is therefore a challenging task. For example, how the texture and taste of beer depend on the foam structure – notably on size and number of bubbles – has only recently been understood[17,18]. Even the surface state of the container plays a role and can contribute to a rapid breakdown of the foam. To further develop on the example of beverages, superamphiphobic surface coatings are used to prevent the formation of unwanted foam during the filling of bottles[19]. Obviously, foams are not limited to beverages, and can be found in many other applications: detergency, food, cosmetic and also for industrial processes such as froth or foam flotation applied for materials or waste recycling, oil recovery from ground, firefighting, mitigation of blast waves from explosions with a very active research in each of these fields nowadays[20–25]. Depending on the application, the desired foam properties might vary considerably. Sometimes, an expanded and stable foam is required, for example in firefighting applications, to create a dense blanket acting as an insulating barrier between the fuel and the air and preventing the development of combustion[26]. Sometimes, as for cleaning, a rather unstable foam that shows better performance in organic compounds dispersion than stable ones, is required[27].

However, the importance of each of the parameters listed above and more especially their coupled influences on the structural evolution of foams remain difficult to quantify because foams are multi-scale structures. The different structural scales of the foam are depicted in Fig. 1 and can be probed using suitable techniques. At the centimetre scale, optical studies provide general information on the foamability, i.e. the amount of gas that can be trapped in a foam. It is also possible to measure the size distribution of gas bubbles[28,29] that create in close contact, when the foam dries, a continuous network of liquid channels (Plateau borders) connected by nodes and thin films. At the bubble scale (>100 µm), this 3D network evolution and connectivity can be understood through foam rheology analysis[30,31]. Foam drainage is primarily governed by the flow of liquid through these channels and nodes and strongly depends on the viscosity of the fluid[32,33]. However, surfactants self-assemblies and other colloidal species (1-10 nm) entrapped in foam will also impact its stability[34,35]. Surface active properties of the foaming agents present at water/air interfaces are at the origin of the stabilization of the gas bubbles and are also determinant in the drying regime liquid drainage. Indeed, when inter-bubble films start to thin, phe-

[a] Institut Max von Laue - Paul Langevin (ILL), 71 avenue des Martyrs, 38042 Grenoble, France.
[b] Université Grenoble Alpes, CNRS, LIPhy, 38000 Grenoble, France
[c] Teclis Scientific, 69380 Civrieux-d'Azergues, France
[d] ICSM, Univ Montpellier, CEA, CNRS, ENSCM, Marcoule, France
[*] chiappisil@ill.eu

nomena of bubble ripening and/or coalescence initiate. Depending on the cohesive interactions between surfactant molecules at water/air interfaces and their dynamical exchange between interfaces and the bulk solution, foam aging can be slowed down or accelerated. Repulsive interactions between facing surfactant monolayers, of electrostatic or steric origin, can also be tuned to counterbalance the capillary pressure that increases as the Plateau borders become thinner and more curved[36]. It is through the succession of film ruptures that the foam collapses. Accordingly, information on the film thickness (< 100 nm), correlated to that at other scales, is crucial for a deep understanding of the stability of the foam.
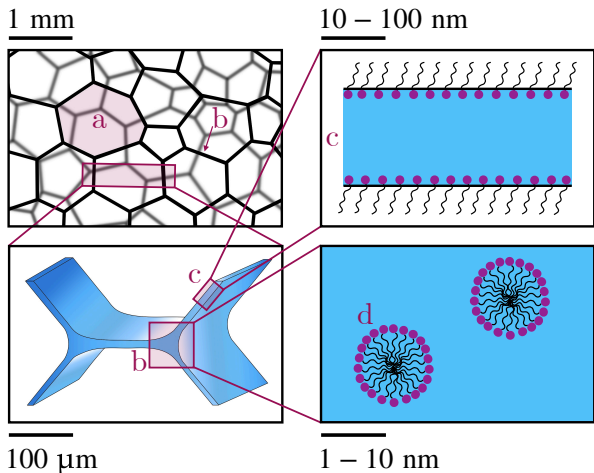

Figure 1: Schematic representation of a liquid foam at different length scales from millimeter to nanometer. The different elements of a foam are identified by a letter: (**a**) a bubble, (**b**) a Plateau border, (**c**) a film/lamella and (**d**) a micelle.

Commercial foam analysers are recurrently used to study foams. They allow liquid foams to be generated by mechanical means – beating or whipping the solution – or by bubbling gases through porous plates. Once generated, various foam structural parameters, such as water volume fraction, foam height, bubble size distribution are followed over time by image processing and electrical techniques. This information, although crucial to probe the foam destabilization mechanism, lack an essential piece of information: the inter-bubble film thickness. A common method to measure it is the Thin Film Pressure Balance. A surfactant film is subjected to an external gas pressure and the difference with the capillary pressure causes the film to drain until the pressures are balanced[37]. The film thickness is then measured by interferometry as a function of the applied pressure to build a pressure isotherm allowing the experimentalist to quantify the interactions between facing interfaces[38,39]. However, these experiments are carried out on isolated films and the extrapolation of these observations to the evolution of the 3D structures such as liquid foams where other effects impact the drainage is far from trivial.

In-situ foam film thickness measurement is possible performing small-angle neutron scattering (SANS)[40–49]. SANS data also provide information on the internal structure of the foam solution over a large length scale. The relatively large diameter of the beam (a few tens of millimetres) allows to probe several hundred bubbles and films. This method therefore provides acceptable statistics on data collected during time scales of minutes, a

sufficient temporal resolution if the foam does not collapse too quickly. A first cell was manufactured in the early 2000s and consisted of a Plexiglas cell with a quartz window allowing the study of foam at a single given height[50]. Since then, interest in this technique has continued to grow with new cells recently developed[51]. The technique has been employed to probe stimuli responsive foams[43,44], foams stabilized by polymeric surfactants[45], proteins[46], or, more recently, nano-ions[48].

While SANS enables to determine with precision the thickness of films in real foams, it is essential to characterise the foam in its entirety and on all its scales simultaneously: from the bubble to the film, in order to optimise the different parameters involved in the ageing of the foam. To address this challenge, we have developed a new device that enables to simultaneously collect microscopic information on the foam via SANS experiments and macroscopic information, with the acquisition of 2D images using an optical camera, as well as conductivity data measured through the foam. Moreover, we have developed an analysis framework to combine the results obtained simultaneously from the different techniques.

In this article, we present the features of this new device as well as the methodology for data analysis. The possibilities offered by the combined analysis is demonstrated using a foam stabilized by a commercial non-ionic polyoxyethylene (10) oleyl ether surfactant (BrijO10) doped with the anionic sodium dodecyl sulfate (SDS) to enhance an electrostatic stabilization of the foam.

2 MATERIALS AND METHODS

2.1 MATERIALS

The non-ionic surfactant BrijO10 ($C_{18:1}E_{10}$) and the ionic surfactant sodium dodecyl sulfate (SDS, $NaC_{12}H_{25}SO_4$, $\geq 99.0\%$) were purchased from Sigma Aldrich. All chemicals were used without further purification. The data presented in this article were conducted with a foam stabilized with 0.5 mM BrijO10 which is well above the critical micelle concentration of 40 µM[52] and upon addition of 0.2 mM SDS. Samples were prepared in Milipore water for Foam-analyser experiments and in D_2O purchased from Eurisotop (99.9% isotopic purity) for small-angle neutron scattering (SANS) experiments. The densities, scattering length densities (SLD) and volumes v for all the chemicals used are given in Table S1 in the electronic Supplementary Material.

2.2 QUARTZ COLUMN

The main part of the new device is a column – entirely made of quartz, a material transparent for neutrons – and designed on the model of the FOAMSCAN from Teclis Scientific (France) in which the foam is formed. This cell, shown in Fig. 2, is cylindrical (30 cm high with an internal diameter of 35 mm and a wall thickness of 2 mm) and is always opened at the top. A flat face was machined in order to glue four prisms at different fixed heights, allowing image capture of the bubbles in contact with the wall. Five pairs of electrodes were also integrated to measure the conductance through the foam at different heights. This cell is therefore compatible with the FOAMSCAN and can be used both in laboratory and on neutron diffractometer dedicated to small-angle scattering technique.

The quartz cell is clipped onto a base via an O-ring to get a set "column and rigid support" tight but easy to dismount for efficient cleaning. The base is composed with a silica frit (pore size 10-16 µm, porosity P16 (ISO 4793)) and can be exchanged
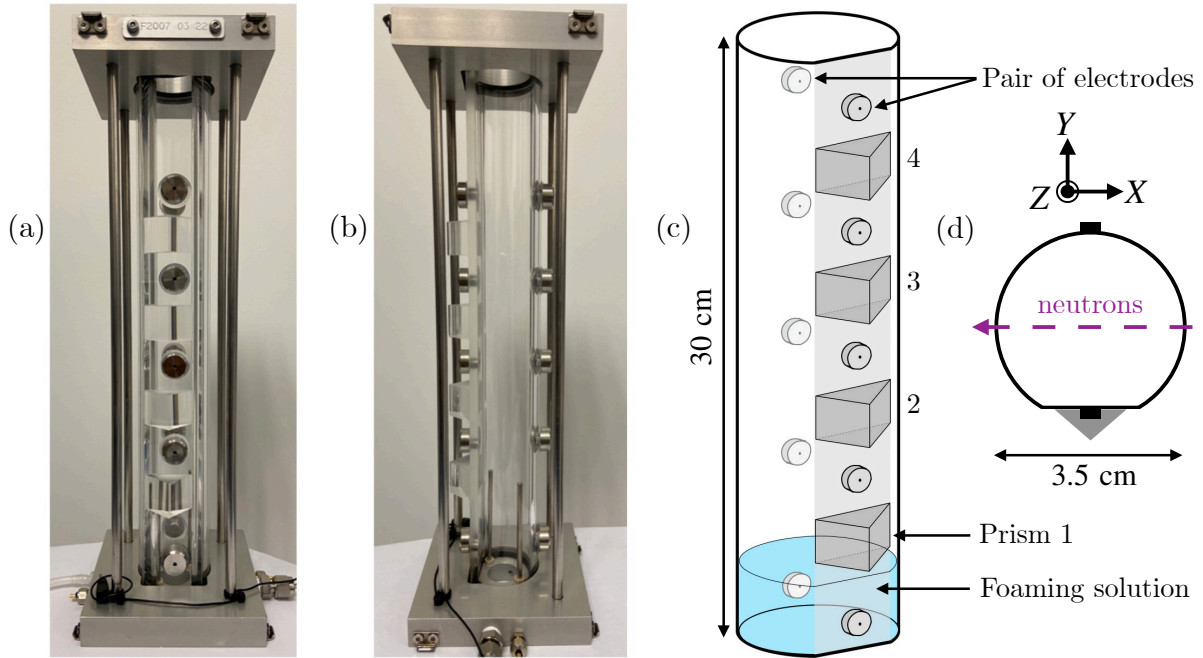
Figure 2: **(a)** Photograph of the quartz cell in front view and **(b)** rotated by 90°. **(c)** Schematic front view and **(d)** top view of the cell. The neutron path is represented with a dotted arrow.

depending on the required bubbling size. The flux of injected gas is controlled by a digital Mass Flow Controller (MFC) from MKS INSTRUMENTS (Andover, Massachusetts, U.S.) with a flow range 0-100 mL/min for model GE50 series. When the foaming solution is injected into the bottom of the column, a slight suppression is maintained to avoid filling the pores of the frit with the solution (with a gas flow rate of 2 mL/min). The foams are then produced with a gas flow rate of 50 mL/min using nitrogen. On the diffractometer, the cell was fixed on a set of Y-Z stages (as showed in Fig. 2d) in order to first center the cylinder in the neutron beam path and second to vary its Z-position so that the neutron beam passes through the cell at heights predefined by the position of the prisms and in order to be able to simultaneously capture photographs of the foam probed by neutrons.

2.3 IMAGE CAPTURE

The photographs of the foam were taken with the acA780-75gm camera from BASLER (Germany). It consists of a Sony ICX415AL CCD sensor with a diagonal of 8 mm and a resolution of 782×582 pixels. A Computar TEC-M55 55mm Telecentric Lens (C Mount) with a focal length of 55mm and an F11 aperture is added to provide a sharp image at a minimum distance of 14 cm. The telecentric lens also allows only light rays parallel to the optical axis to be selected. The light source and camera are located on either side of the prism, at an angle of 45° to the column wall. This experimental method allows to visualize only the layer of bubbles located against the inner wall of the column. In the images, the bubbles appear white and the dark part correspond to the Plateau borders[53]. The scaling calibration is done with a calibrated steel ball, 2 mm, fixed in a mobile support that can be placed in front of the prism before starting the photographic captures.

2.4 CONDUCTANCE MEASUREMENTS

Electronic conductivity measurements were performed using a EPU 452 Quad Multi Function isoPod developed by eDAQ (Colorado Springs, CO, US) and configured to measure ionic conductance $G = k\sigma$. The cell-constant k in cm only depends on the distance between the electrodes and the surface area of the electrodes, which are equivalent for each position of the electrodes pairs.

2.5 SMALL-ANGLE NEUTRON SCATTERING (SANS)

Small-angle neutron scattering (SANS) experiments were performed at room temperature on the D33 diffractometer[54] at Laue-Langevin Institute (ILL) in Grenoble. We opted for the monochromatic mode with a wavelength $\lambda = 6$ Å. The detector consists of a central panel set at 10 m and 4 side panels set at 1.7 m. The collimation length was set to 12.8 m and the beam size at the sample position was fixed at 15 mm in diameter. Under these conditions, the accessible scattering vector q range, with q defined as $q = 4\pi \sin(\theta/2)/\lambda$, varies from 0.002 to 0.25 Å^{-1}. The neutron beam was set at the same height as the camera to correlate the various collected data. Acquisition time was fixed at 60 s for scattering data and 30 s for transmission data. Normalization and azimuthal averaging of the 2D-data was applied using the GRASP software package[55]. The empty cell signal was subtracted for each scattering curve. Absolute scale was obtained by normalizing for the neutron beam flux. The experiments described in this article were performed at the height of the second prism, at 8 cm above the level of the solution at rest. SANS experiments were also conducted on foaming solutions in quartz cuvette of 2 mm thick on the D22 diffractometer to obtain structural information of micellar solution. In this configuration,

neutron wavelength was also set at 6 Å and with two detector distances at 1.4 and 17.6 m and with a 17.6 m collimation, resulting in a q-vector range from 0.003 to 0.64. Å^{-1}.

2.6 Foam generation and aging procedure

Prior to SANS measurements, foams were studied using the FOAMSCAN apparatus and by injecting 40 mL of the foaming solution into the column in 10 mL steps through the inlet at the bottom of the column, just above the frit. After each injection step, the conductance was measured, resulting in a linear calibration curve (conductance versus liquid volume). Then, N_2 was flowed at 50 mL/min through the porous frit. Once the column was filled by the foam, the N_2 flow was stopped leaving the foam under free drainage conditions during 2 to 3 hours. The foam structure was captured using one camera when using the FOAMSCAN. The sample was analysed 3 times from a fresh foaming solution. The quartz column was rinsed generously with Millipore water and dried after each test. The SANS experiments were performed using the same procedure: after stopping the gas flux, the evolution of the foam was followed using simultaneously conductivity , imaging, and SANS techniques for 75 minutes.

2.7 Surface Tension measurement

The surface tension of the surfactants at the air-water interface was measured at room temperature using a Tracker developed by Teclis Scientific. The measurement of surface tension was performed on bubbles of 5 µL during 10 min. This measurement was repeated 3 times.

3 Data analysis procedure

3.1 Data collection

The foam is generated in the quartz cell from the foaming solution containing the nonionic surfactant Polyoxyethylene (10) oleyl ether (Brij O10) at 0.5 mM doped with 0.2 mM sodium dodecyl sulfate. The molar ratio of anionic to nonionic surfactant is $1/2.5$. The gas flow is stopped once the column is filled, defining the starting point $t = 0$ of the time-resolved experiments. The structure of the foam is then investigated as a function of time at the level of the prism 2 for this study, at approx. 8 cm above the liquid surface. Fig. 3 presents a typical set of kinetics data recorded simultaneously during the free drainage of a foam: 2D SANS scattering data (Fig. 3a and 3c) with the corresponding radially averaged scattering curves (3f), 2D optical images of the foam (Fig. 3b and 3d), and conductance values recorded on electrode pairs below and above the prism 2 (3e).

3.2 Image processing

The collected optical images were binarised to extract the relevant information: bubble size, liquid volume fraction, specific surface area of the foam and the radius of the Plateau borders. This binarisation process was automated using the "Adaptive Threshold" command from OpenCv package[56], which determines a different threshold value for each pixel depending on the grey level of its neighbourhood. Once the image is binarised, "findContours" and "drawContours" commands from OpenCv package[56] are applied to remove artefacts from impurities within the bubbles. The source code used for the image treatment is provided in section S2 of the Supplementary Material.

From the binarised images, the surface area of each bubble in contact with the wall of the column S_{bubble} was measured as well as their surface radius expressed as $r = \sqrt{S_{bubble}/\pi}$. The distribution of the radii can be characterized by the Polydispersity Index PI expressed as

$$PI = \frac{\sqrt{\langle r^2 \rangle - \langle r \rangle^2}}{\langle r \rangle}. \tag{1}$$

If PI is greater than 0.2, it was demonstrated through simulations that the distributions of the surface radii are well correlated with those of the 3D bubbles[57]. Since for the investigated system we found $PI > 0.37$, we no longer distinguish between surface radius and volume radius.

From the foam images, the liquid fraction ϕ is also determined as a function of time. Its estimation is based on the calculation of the surface fraction ϕ_s, expressed as the ratio between the area of the pseudo Plateau borders A_{PB} – that corresponds to the number of black pixels after binarization – and the total area of the foam A_{foam}: $\phi_s = A_{PB}/A_{foam}$. By considering the foam as a network of liquid channels with a characteristic length close to the bubble radius, a relationship exists between ϕ_s and ϕ using the following equation[58]:

$$1 - \phi_s = \left(1 - \sqrt{\frac{\phi}{\phi_c}}\right)^2 \tag{2}$$

where ϕ_c is the critical liquid fraction, which is close to 0.36 in the case of a polydisperse foam[58]. An uncertainty on these data can be determined by taking into account that the threshold value chosen for the binarization will modify the quantity of black pixels and thus the value of the liquid fraction. To estimate the dispersity of this value, different threshold values were tested.

The specific surface area of the foam, i.e. the ratio of the total surface area of the water/air interfaces over the total volume of foam, can also be estimated by image analysis. The model holds for dry polydispersed foams, where the surface size distribution obtained from the images represents the true bulk polydispersity of the foam. In such a case, the specific surface area of the foam can be approximated by:

$$\left.\frac{S}{V}\right|_{img} \simeq \frac{l_{PB}}{S_{photo}} = \frac{N_{black}}{N_{total} \times l_{1px}} \tag{3}$$

with l_{PB} the total length of all Plateau borders in the picture, S_{photo} the area of the picture. After applying a topological skeleton process to reduce Plateau borders to single-pixel-wide shapes (see section S2 in the Supplementary Material for more information), the specific surface is equal to the ratio between the number of black pixels N_{black} and the number of pixels of the image N_{total} multiplied by the side-length of one pixel $l_{1px} = 1.2 \cdot 10^{-3}$ cm. The uncertainty of the data is obtained by applying the same skeletonization procedure, but using a different image processing program, ImageJ.

It is also possible to extract the radius of the Plateau borders r_{PB} from the binarised and skeletonized images. The analysis method is detailed in section S2 of the Supplementary Material.

3.3 Conductance data

The liquid fraction ϕ is also determined using electrical conductance values for comparison with those determined by using image analysis. The following empirical relation is valid for both
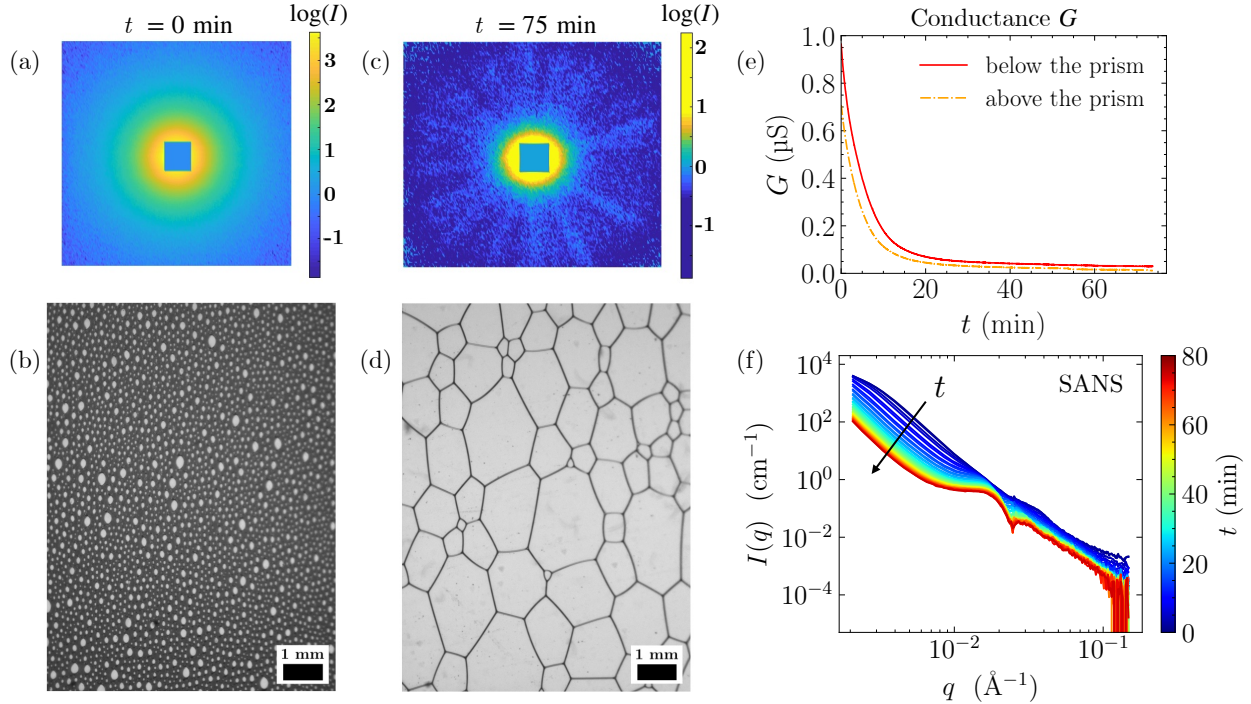
Figure 3: Classic set of experimental data with an example of 2D SANS data on the central detector (**a** and **c**) at the beginning and at the end of the experiment respectively and corresponding photograph of the foam taken at the level of prism 2 (**b** and **d**). (**e**) Time dependence of the conductance G measured on the pair of electrodes below and above prism 2. (**f**) Radially averaged SANS data as a function of time from blue, $t = 0$ min to red, $t = 75$ min. The arrow is in the direction of increasing time.

wet and dry foams:[59]

$$\phi = \frac{3\sigma_r(1 + 11\sigma_r)}{1 + 25\sigma_r + 10\sigma_r^2} \quad (4)$$

with $\sigma_r = \sigma_{\text{foam}}/\sigma_{\text{liquid}}$ the ratio between the measured conductivity through the foam and the liquid. The ratio of conductivities σ_r can be approximated by the ratio of conductances $G_r = G_{\text{foam}}/G_{\text{liquid}} = k\sigma_{\text{foam}}/k\sigma_{\text{liquid}} = \sigma_r$ since the constant cell k is similar at all heights of the cell. For the BrijO10+SDS solution, the conductance measured at the bottom of the cell is equal to $G_{\text{liquid}} = 10.5$ µS. As can be seen in Fig. 3e, since the electrodes are located below and above the prism, the conductivities are averaged to provide the value of ϕ at the height of the neutron beam.

3.4 SANS DATA ANALYSIS

A third approach was followed to study the liquid volume fraction evolution applying the Beer–Lambert law from the neutron transmission values and using 1.549 cm as adsorption length for D_2O[60]. The uncertainty on the transmission ΔT related to the counting statistic of the 2D detector is propagated to obtain the uncertainty on the liquid fraction. The transmission value measured at 6 min is equal to 0.85 and is higher than 0.99 after 17 min. The values are high enough to safely neglect multiple scattering.

In addition to the determination of the liquid fraction of the foam, small-angle scattering is mainly employed for the microstructural characterization of the foam. In particular, given the large size of the neutron beam (15 mm diameter), the large

sample thickness (3.5 cm), and the relative small size of the bubbles ($\sim$ 1 mm), isotropic scattering patterns are obtained throughout the drainage, except at the end of the sequence when the foam is very dry. Given the fact that the characteristic sizes associated to the different contributions strongly differ – a few nm for the micelles, a few tens of nanometers for the films, several µm for the Plateau borders – the azimutal averaged SANS intensities can be analysed as the coherent sum of different contributions.

3.4.1 CONTRIBUTION OF MICELLES

The micelles within the Plateau borders will contribute to the total scattering intensity. Herein, we assume that size, shape and concentration of micelles within the Plateau borders are exactly equal to those of the micelles in the foaming solution. The latter was thus investigated separately to determine the micellar structural parameters and the intermicellar interactions used to compute the scattering form and and structure factors, respectively. A model of core-shell ellipsoidal micelles interacting via a charged hard sphere potential was used. Full details are provided in the section S3 in the electronic Supplementary Material. The contribution of the micelle scattering is described as:

$$I_{\text{micelle}}(q)[\text{cm}^{-1}] = {}^1N \cdot \phi \cdot P_{CS}(q)S_{\text{cHS}}(q) \quad (5)$$

with ${}^1N$ the particle number density in solution, ϕ the liquid fraction in the foam, $P_{CS}(q)$ the scattering form factor and S_{cHS} the scattering structure factor (see electronic Supplementary Material). Under the aforementioned assumptions, only the liquid fraction ϕ of the solution within the foam remains an adjustable

parameter and will be compared and discussed with respect to the liquid volume fractions determined using the other complementary analysis.

3.4.2 Contribution of Plateau borders (PB)

At q values below $5 \cdot 10^{-3}$ Å^{-1}, a scattering intensity decay close to q^{-4} power law is clearly visible for both wet and dry foams. The q^{-4} signal in SANS is characteristic of well-defined interfaces scattering and described by the Porod law[61]. These interfaces of characteristic size $d \gg 0.125$ µm can be associated to the network of Plateau borders. The scattering intensity applied to air-D_2O system is expressed as:

$$I_{PB}(q)[\text{cm}^{-1}] = 2\pi\Delta\rho^2 \left.\frac{S}{V}\right|_{PB} \frac{1}{q^4} \tag{6}$$

where $S/V|_{PB}$ the specific surface area of the Plateau borders and $\Delta\rho^2$ the difference in scattering length density of D_2O and air.

3.4.3 Contribution of lamellae

The other major structural component of foams are the foam films between adjacent bubbles. For sufficiently dry foams, the foam bubbles are polyhedral[62]. For the sake of simplicity, to calculate the contribution of the scattering from the foam lamellae, the system is modelled as a collection of randomly oriented large discs of radius r. A schematic representation is given in Fig. 4a. Hereafter, two approaches to compute the scattering intensity are presented.
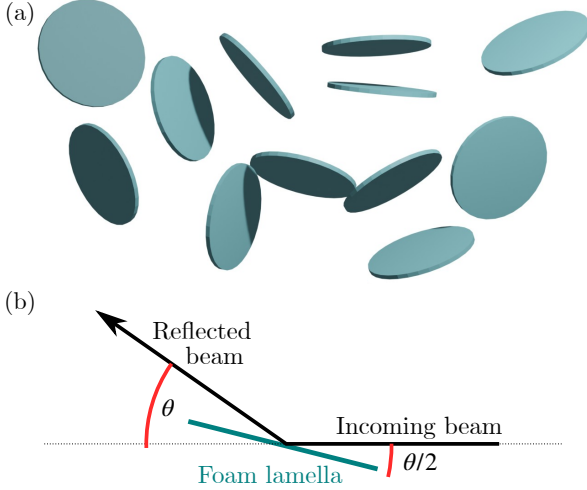

Figure 4: **(a)** Schematic representation of a collection of randomly-oriented discs simulating the flat interbubble films. **(b)** Schematic representation of the reflectivity process at an angle θ from one disc satisfying the specular condition.

In a first approach, the contribution of the foam films is calculated considering scattering from flat discs of radius r and thickness h, i.e., with $h \ll r$:[63]

$$I_{lamellae}^{scatt}(q)[\text{cm}^{-1}] = 8^1N_{tot}\Delta\rho^2 \frac{(\pi r^2 h)^2}{(qr)^2} \frac{1 - J_1(2qr)}{qr} \frac{\sin^2\left(\frac{qh}{2}\right)}{(qh)^2} \tag{7}$$

where J_1 is the first-order Bessel function, and the scattering contrast $\Delta\rho$ the difference in scattering length density of D_2O and air. The radius of the disk for the fit was set to $r = 0.1$ mm, ($q = 2\pi/r = 10^{-6}$ Å^{-1}). The macroscopic value for the lamellae size was chosen not to have an impact on the modeled SANS curve within the measured q range ($q \in [5 \cdot 10^{-3}; 2 \cdot 10^{-1}]$ Å^{-1}). The lamellae number density $^1N_{tot}$ is related to the foam specific area as:

$$^1N_{tot} = \frac{S/V|_{film}}{\pi r^2} \tag{8}$$

with $S/V|_{film}$ being the specific surface of the foam films. Accordingly, the only adjustable parameters are the specific foam film surface $S/V|_{film}$ and the foam film thickness h. This equation is obtained within the Born approximation[64], i.e. the amplitude of the incident wave remains constant through the scattering object. This implies that the scattered or adsorbed intensity is negligible with respect to the transmitted one. While the Born approximation is at the basis of the vast majority of small-angle scattering analyses, this model is not able to describe our experimental data around 0.15 Å^{-1}, as shown in Fig. 5a with a pseudo plateau that is reinforced as the foam is drying. The oscillations and the plateau in the intensity curve cannot be described considering the scattering contribution of the lamellae in addition to the contribution of the Plateau borders and of the micelles, as shown in Fig. S4 in the electronic Supplementary Material. According to recent publications on foam small-angle scattering[65], this plateau appears to correspond to the reflectivity plateau of a air/D_2O/air film of several nm thickness. We can consider that the large foam films give rise to a specular reflection signal, provided the specular condition – the incidence angle equals the reflection angle – is met, as shown in Fig. 4b. Thus, the Born approximation does not hold below the critical angle, where every neutron is reflected, and thus, the typical small-angle scattering formalism cannot be employed for taking into account for the thin film scattering contribution.

Thus, in a second approach, we assume that the disks are large and flat, compared to the neutron coherence length, and so a specular reflection of the air/D_2O/air interface takes place. From the definition of the scattering intensity, it follows that:

$$I_{lamellae}^{reflec}(q)[\text{cm}^{-1}] = R(q, h, \Delta\rho, \sigma)\frac{A(\theta)}{A_0}\frac{1}{T\Delta\Omega} \tag{9}$$

with $R(q, h, \Delta\rho, \sigma)$ being the probability of a neutron being reflected at a given scattering vector, $A(\theta)$ the projected area of the foam on the beam-axis, A_0 the area of the neutron beam, T the sample thickness, and $\Delta\Omega$ the solid angle. $R(q, h, \Delta\rho, \sigma)$ is computed according to the Parratt formalism assuming a layered air-D_2O-air system with a thickness h, roughness σ, with $\Delta\rho$ the difference in scattering length density of D_2O and air. Provided the very low roughness characterizing the foam films, off-specular reflection is neglected. The solid angle is given by:

$$\Delta\Omega = 2\pi\sin\theta\Delta\theta \tag{10}$$

The projected area of the foam on the beam-axis is given by:

$$A(\theta) = N_{spec}\pi r^2 \sin(\theta/2) \tag{11}$$

with πr^2 being the area of one lamella, and N_{spec} the number of lamellae satisfying the specular condition. We assume that the lamellae are randomly oriented and thus the fraction of lamellae satisfying the specular condition depends on the beam divergence θ_{div} as:

$$N_{spec} = N_{tot}\frac{\theta_{div}}{\pi} \tag{12}$$

Substituting Eqs. 10 - 12 in Eq. 9, one obtains:

$$I_{\text{lamellae}}^{\text{reflec}}(q)[\text{cm}^{-1}] = R(q, h, \Delta\rho, \sigma) \frac{N_{\text{tot}} \pi r^2 \ (\theta_{\text{div}}/\pi) \ \sin(\theta/2)}{T \ A_0 \ 2\pi \sin\theta \Delta\theta}$$

(13)

which, in the small-angle approximation ($\sin(x) \approx x$), simplifies to:

$$I_{\text{lamellae}}^{\text{reflec}}(q)[\text{cm}^{-1}] = R(q, h, \Delta\rho, \sigma) \frac{^1 N_{\text{tot}} \ r^2 \ \theta_{\text{div}}}{4\pi \ \Delta\theta}$$

(14)

with $^1 N_{\text{tot}} = N_{\text{tot}}/(TA_0)$ being the number of lamellae per scattering volume. If $\Delta\theta$, arising from the definition of the solid angle is approximated with the beam divergence, Eq. 14 further simplifies to:

$$I_{\text{lamellae}}^{\text{reflec}}(q)[\text{cm}^{-1}] = \left.\frac{S}{V}\right|_{\text{film}} \frac{R(q, h, \Delta\rho, \sigma)}{4\pi^2}$$

(15)

By adding the specific surface of the films $S/V|_{\text{film}}$ and that of the Plateau Borders $S/V|_{\text{PB}}$ allows us to estimate the total specific surface of the foam $S/V|_{\text{foam}} = S/V|_{\text{PB}} + S/V|_{\text{film}}$. This provides an elegant relationship between the measured scattering intensity, the reflectivity signal and the foam area per unit volume. Accordingly, through eqs. 9-15, a formalism to relate the reflection signal arising from the foam film in absolute units was derived. As shown in Fig. 5a, the intermediate range of the scattering data can be described using "reflectivity" approach.

To confirm that the difference between the calculated "scattered" (Eq. 7) vs. "reflected" (Eq. 15) wave comes from the different formalism used to derive the two calculated curves, the reflectivity signal was also calculated within the Born approximation. For a thin film of thickness h of D_2O in air, the reflected intensity calculated within the Born approximation is given by[66]:

$$I_{\text{lamellae}}^{\text{reflec,Born}}(q)(q, h, \Delta\rho)[\text{cm}^{-1}] = \frac{1}{4\pi^2} \left.\frac{S}{V}\right|_{\text{film}} \frac{16\pi^2}{q^4} (2\Delta\rho)^2 \sin^2\left(\frac{qh}{2}\right)$$

(16)

The three calculated curves overlap at high-q (Fig. 5a), within the validity of the Born approximation, while they significantly differ at small angles. In particular, only the reflectivity signal without the Born approximation is able to correctly describe the pseudo plateau in scattering data. It is also noteworthy that the spacing between the minima differs according to the model used in the intermediate q region. In particular, the position of the first minimum in the reflectivity curve depends not only on the film thickness but also on the scattering length densities (SLD). This implies that the determination of the foam film thickness from the position of the oscillation can be reliably performed only if three or more oscillations are present in the data.

Fig. 5b shows the different contributions and the resulting intensity for a dry, 65 minute old foam, taking into account the Porod scattering from the Plateau borders, the reflection at the foam-film interface without Born approximation, and the scattering of the micellar aggregates presents in the foam channels. While several examples dealing with the analysis of SANS data from liquid foams can be found in the literature[40–46,48,49], this is the first example of a quantitative analysis, in absolute scale, of the scattering data recorded from liquid foams. The fitting procedure was done considering a film roughness of $\sigma = 1.5$ nm. There are only 4 parameters that are adjusted during the fit procedure: the liquid fraction ϕ, the film thickness h, and the specific surface area of the films $S/V|_{\text{film}}$ and of the Plateau borders $S/V|_{\text{PB}}$. The values obtained for the foam shown in Fig. 5b, at 65 min, are $\phi = (2.5\pm0.5)\%$, $h = (40\pm3)$ nm, $S/V|_{\text{PB}} = (6.1\pm0.1)$ cm^{-1} and $S/V|_{\text{film}} = (14.3\pm0.5)$ cm^{-1}. Such information is not available by any other technique.
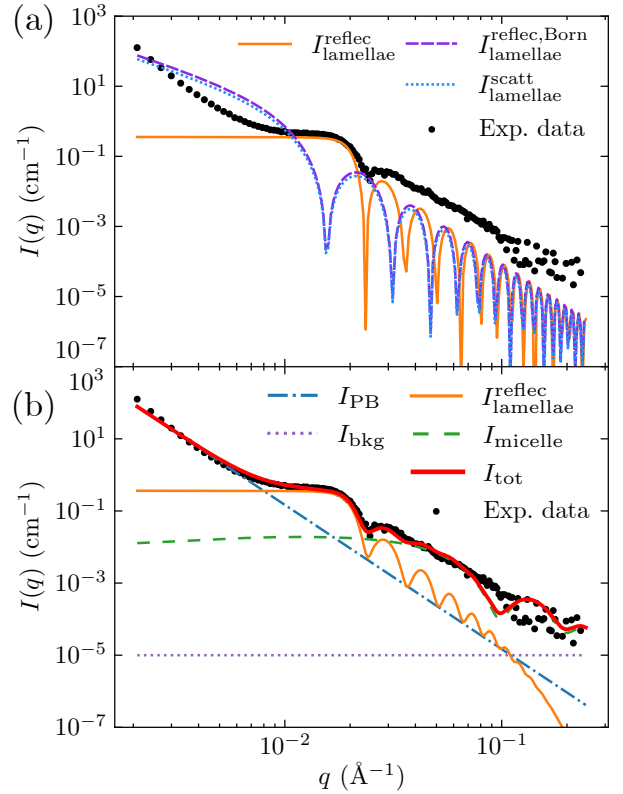

Figure 5: **(a)** Foam scattering data collected at 65 min of aging to which are superimposed either scattering intensity from ramdomly-oriented discs (eq. 7) or reflectivity signal within (eq. 16) or without (eq. 15) the Born approximation from the same set of discs without taking into account a surface roughness. **(b)** Same data adjusted with a model at three contributions: I_{PB} from Plateau borders, I_{micelle} from micelles present within the foam and $I_{\text{lamellae}}^{\text{reflec}}$ from discs considering the reflectivity assumption according to Eq. 15 with a film roughness $\sigma = 1.5$ nm. I_{bkg} is the incoherent scattering background.

4 RESULTS

Hereafter, the stability of a nonionic/anionic surfactant stabilized foam is investigated by following the foam volume, the bubble size distribution, the specific surface area, the liquid fraction and the lamellae film thickness as a function of time. The goal of this case study is to provide the reader with an overview of the information that can be extracted from this multi-method approach coupled with suitable data analysis.

4.1 MACROSTRUCTURAL CHARACTERIZATION

The evolution of the foam volume is shown as a function of time in Fig. 6 and three regimes can be identified. First, in regime 0, the foam rise phase corresponds to the generation of foam, with the foam filling the column. Under the given conditions, the column is filled after 4 minutes. In parallel, the volume of the sub-phase solution is decreasing (dotted red curve in Fig. 6). Once the gas flow is stopped, the foam then evolves through a free drainage process (phase I and II). During phase I, the kinetic of drainage is fast and water trapped within the foam drains through the Plateau borders with a drainage front which shifts downwards at constant velocity[36]. The volume of the foam decreases and

reaches an inflection point that defines phase II. It has to be noted here that the decrease in foam volume, associated to the drainage of the liquid solution, takes place at the bottom of the foam, and that the total volume of the system, {foam + liquid solution}, remains relatively constant in this phase. Once the excess solution has drained within the foam, the second phase of foam aging, much slower, begins. In this phase, the interlamellar interactions and capillary forces act against the gravity. This stage is characterized by a pseudo-plateau in the foam volume variation, which ends, in the investigated system, at approx. 30 minutes. At this stage, the foam at the top of the column is very dry; the bubbles start to break and the foam gradually collapses.
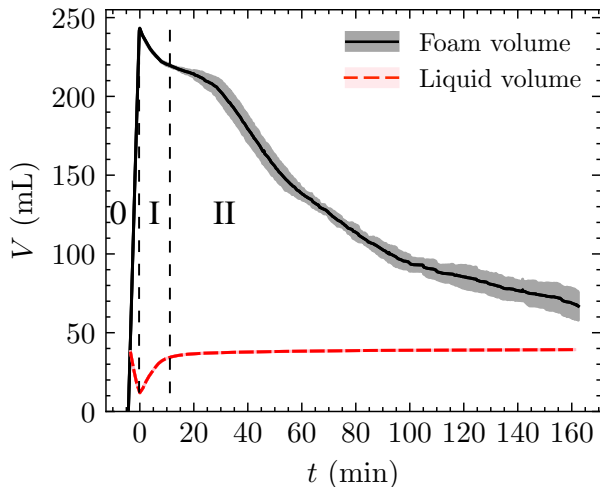

Figure 6: Foam volume (black line) and solution at th bottom of the column (dotted red line) as a function of time. The respective standard deviations are plotted as shaded region from three independent measurements using the Foam-analyzer. The liquid volume error bars are too small to be visible. Time phase 0 corresponds to the foam generation phase. Time $t = 0$ corresponds to the end of foaming. Phases I and II corresponds to aging phases during the free drainage.

While the foam volume evolution provides a general overview over the foam stability, the simultaneous recording of foam photographs, electrical conductivity, and small-angle neutron scattering patterns allows us to get a deeper structural understanding of the foam ageing mechanisms.

4.1.1 Bubble size distribution

Representative pictures of both a humid foam and a dry one are given in 3b and 3d, respectively, and all photos taken of the foam are shown in Fig. S5 in the Supplementary Material. The mean size, polydispersity index of the foam bubbles, radius of the Plateau borders as well as the liquid fraction were analysed according to the procedure described in section 3.2 and the results of their time evolution are shown in Fig. 7.

The mean radius $\langle r \rangle$ increases from 0.04 to 0.43 mm with a slight inflection in its evolution around 40 min. The PI of the distribution increases quickly from 0.37 to 0.58 in the first 10 min to be then almost constant, whereas the number of bubbles N decreases continuously as a function of time. The radius of the Plateau borders decreases until reaching a plateau around 20 min. The increase in the radius of the bubbles over time as well
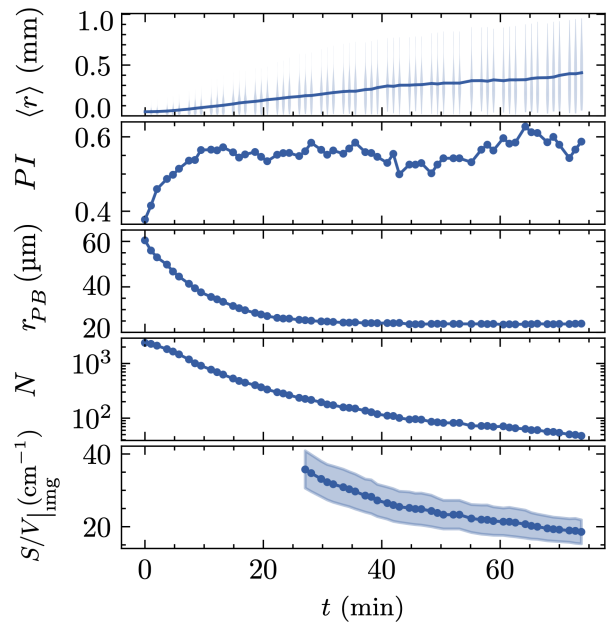

Figure 7: Evolution of the average radius of the bubbles $\langle r \rangle$, of the polydispersity index PI, of the radius of the Plateau borders r_{PB}, of the number of bubbles N and of the total specific surface area of the foam $S/V|_{\mathrm{img}}$ as a function of time, measured by the analysis of the images obtained during the SANS experiments. The probability density is plotted along the y axis as a "violin diagram". Error bars are represented as a shaded area. The model that determines the specific surface requires a very dry foam, which explains the absence of points below 20 min.

as the decrease of N mean that coalescence and coarsening play a role in the decay of the foam as expected, but with a kinetics that remains slow.

4.1.2 Liquid fraction

To obtain information about drainage, the time evolution of the liquid fraction ϕ was also determined. As mentioned previously, four independent techniques were used: conductance measurements, image analysis, neutron beam transmission and SANS data analysis. The data from the first three techniques are given in Fig. 8a.

Although slight differences are visible, the three methods are consistent and provide a clear trend for the evolution of the liquid volume fraction in the foam as a function of time. These three methods have different strengths and weaknesses to estimate the liquid volume fraction within the foam at a given height: electrical conductivity is a reliable and robust method, but it can be applied to conductive solutions only; ϕ obtained from the image analysis suffers from the choice of the threshold during the binarization procedure and is limited by the camera resolution. However, it can be applied to any foam, even non-ionic ones. Neutron transmission suffers from low signal-to-noise ratio and although the measurements are taken primarily to obtain absolute units of the SANS data they are also used in this context to corroborate the correctness of the solution volume fraction at a given height in the foam and as a function of time. As mentioned, all three methods give similar results and make it possible to determine the time evolution type of the foam quality: wet foam
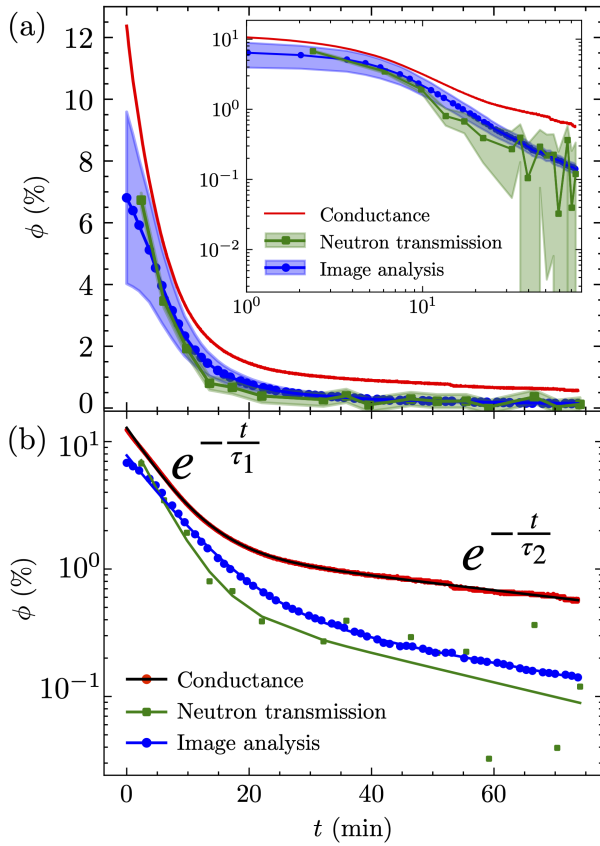
Figure 8: **(a)** Determination of the liquid fraction ϕ at the height of prism 2 from mean conductance measurements on the electrode above and below the prism (red curve), from collected photo-images on the prism 2 (blue curve), and from transmission of the neutron beam (green curve). The data are plotted in log-log scale in the inset. Error bars are represented as shaded regions. **(b)** The same data (dots) are plotted in log-linear scale and fitted using a bi-exponential decay represented by the lines (black, blue and green).

($\phi > 10\%$), dry foam ($\phi < 5\%$) or very dry foam ($\phi < 1\%$). The evolution of the liquid fraction determined by these three methods shows a bi-exponential decay:

$$\phi(t) = A\exp(-t/\tau_1) + B\exp(-t/\tau_2) \qquad (17)$$

(see Fig. 8b). The characteristic times τ_1 and τ_2 obtained by the different methods are in good agreement around 5 min and 1 h respectively and are given in Table 1. It is shown that the drying of the foam in this example takes place in two steps, a fast one with a characteristic time of few minutes, followed by a slower one of approx. 1 hour.

4.2 MICROSTRUCTURAL CHARACTERIZATION OF THE FOAM

As detailed previously, SANS experiments were performed during foam aging to obtain microstructural information of the foam as a function of time. The SANS analysis model was applied to all the recorded scattering curves as shown in Fig. S6 in the Supplementary Material. However, the SANS patterns of the young, wet foam (before 10 minutes), could not be fitted assuming specular

	τ_1 (min)	τ_2 (min)
Conductance	5 ± 1	77 ± 1
Neutron transmission	4 ± 2	40 ± 20
Image analysis	7 ± 1	51 ± 2

Table 1: Characteristic decay times and their uncertainties for the liquid fraction time-variation according to the three techniques used.

reflection at the air/D_2O/air interface. At this stage, owing to the high liquid fraction (around 5 %), the surfaces are too curved to provide a reflectivity signal. Between 10 and 20 min, the total reflectivity signal is visible in the experimental data. However, no Kiessig fringes, arising from the interference between the two interfaces of the film, are observed presumably due to the large film thickness or thickness polydispersity. Accordingly, the data between 10 and 20 min were fitted assuming a "thick" film of 60 nm. This dimension has, however, no real physical meaning. While the thickness of the foam films cannot be determined, this approach allows us to calculate the specific surface of the films from the intensity of the reflected signal below the total reflection angle q around 0.15 Å^{-1}. From 20 min onward, all structural parameters – the liquid fraction ϕ, the inter-bubble film thickness h, the specific surface areas from the Plateau borders $S/V|_{\text{PB}}$ and from the films $S/V|_{\text{film}}$ – can be obtained from the fit of the SANS data, and are shown in Fig. 9.
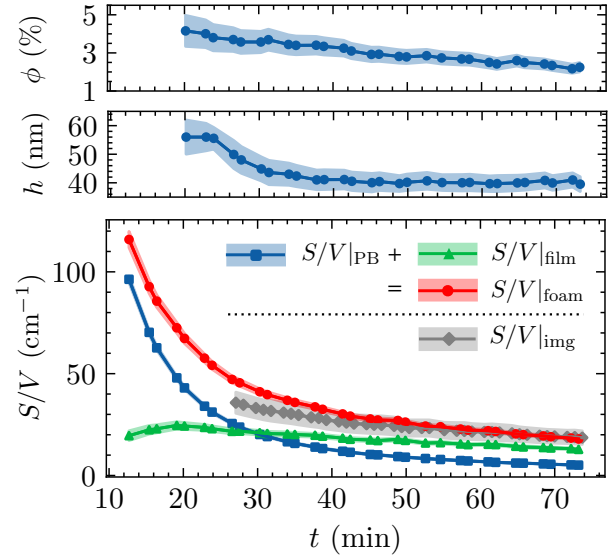

Figure 9: Time evolution of the liquid fraction ϕ obtained from the small-angle scattering of the micelles (Eq 5), the inter-bubble film thickness h and the specific surface S/V obtained from the reflectivity contribution from the thin films (Eq. 15). The total specific surface area of the foam $S/V|_{\text{foam}}$ is obtained by summing the surface area from the Plateau borders $S/V|_{\text{PB}}$ and from the films $S/V|_{\text{film}}$. Error bars are represented as shaded regions and are obtained by minimising the residual error using the least squares method. The specific surface area obtained from image analysis $S/V|_{\text{img}}$ is also plotted for the sake of comparison.

The liquid fraction obtained from the SANS analysis varies from 4 down to 2% in this time range. It appears to be overestimated compared to the values determined using conductance,

neutron transmission, and image analysis. This indicates that either the concentration of micelles in the foam is higher than in the bulk solution, or that the micellar aggregates are larger in the foam than in the solution. We refrain from further investigating the variation of the shape/size/concentration of the micellar aggregates in the foam since, despite being a fundamentally interesting observation, it exceeds the scope of this work. We only hint that performing contrast variation experiments would allow probing the structure of colloidal assemblies within the foam with high accuracy.

As soon as the Kiessig fringes are observable, the foam film thickness decreases from about 55 nm down to 40 nm a value which remains constant over the last 30 minutes of the experiment. These values are in the range of what has been determined using a thin film pressure balance technique on single film submitted to an external pressure before rupture, but still much thicker than Newton or black films. Finally, the last microscopic features are the specific areas from Plateau borders and foam films. Their sum agrees very well with the results from the image analysis, at least in the last 30 minutes, supporting the use of the absolute scale in scattering experiment. In particular, the analysis of the SANS data allows us to discern directly between both specific surface areas. While the surface area of the foam film decreases only moderately with time, the Plateau border area decreases significantly within the investigated time range, from 100 to less than 10 cm^{-1}. The Plateau borders specific surface area decreases with a bi-exponential law (see Fig. S7 in the Supplementary Material), with characteristic times of (7 ± 1) and (42 ± 2) minutes. In contrast, the specific surface area of the films decreases slowly, mostly linearly in time. Then the sum is dominated by the Plateau borders contribution at the beginning of the drainage and then by the foam film at long time aging when the foam is dried.

5 Discussion

As soon as the foam is formed, in the example presented here, the liquid structure is immediately subjected to free drainage which will contribute to its destabilisation. During the first drainage stage, water drains rapidly through the foam with a drainage front that moves downward to reach the foam/solution interface within a characteristic time of approximately 3 min in this geometry and formulation. For times larger than this characteristic time, the entire foam structure relaxes into an aging phase for which the gravity is not the only force acting on the liquid. This time phase corresponds to the pseudo plateau observed around 10 min in Fig. 6. The foam becomes dry with a liquid fraction $\phi < 5\%$. It is interesting to note that during this first phase, the PI of the bubbles radius increases significantly to achieve a quasi constant and large value of about 0.57 during foam aging, in a second phase. This second phase in the foam aging observed in this system corresponds to a much slower process characterized by a set of bubbles that become faceted. The signature of this evolution can be followed by the fluctuations of the scattering intensity, which increase in number and amplitude, start to be detectable on the 2D-detector (see Figs. S8 and S9 in the Supplementary Material)[67]. The bubble size variation first follows a quasi-proportional time law (proportional to t^{β} with $\beta < 1$) and then a trend close to $t^{1/2}$ at long time (see Fig. S10 in the Supplementary Material), an evolution characteristic of a coarsening process[68]. The specific surface area of the foam decreases, mainly due to the decrease in the specific surface area of the

Plateau borders contribution, until the one of the film becomes predominant. In this first part, the capillary suction from the Plateau border channels is significant on the inter-bubbles films. The film thickness decreases until a quasi-constant value. This value is tuned by a balance between the gas pressure in bubbles and the sum of the liquid pressure in Plateau border and within the film (the disjoining pressure) that prevents further thinning of the film and ensures mechanical resistance to coalescence and to coarsening. Indeed, a thickness of 40 nm is still sufficient to prevent or slow down the gas diffusion through the film and the probability of film rupture due to buckling fluctuations and pore formation. Determining roughly the Plateau borders radius from image analysis, of about $r_{PB} = 24$ μm in this second temporal phase and with the measurement of the surface tension in this system, equal to $\gamma = 32$ mN/m, it is possible to estimate a disjoining pressure – defined for a dry foam[36] as $\Pi_d \simeq \gamma/r_{PB}$ – of about 1350 Pa at the end of the experiment. This pressure value in regard to the film thickness is reasonable if it is compared to the values measured for SDS by varying the ionic strength[69].
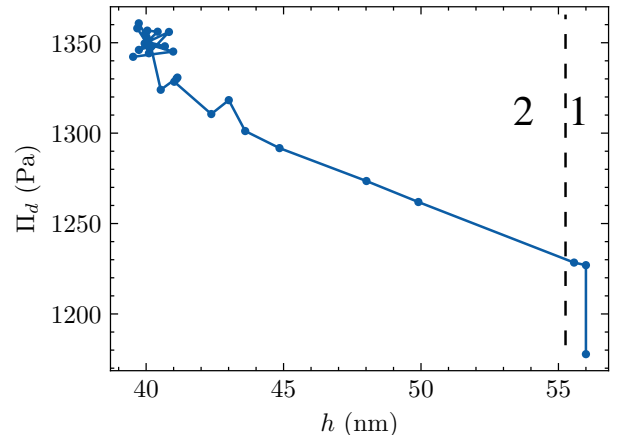

Figure 10: Disjuction pressure Π_d calculated from the values of the Plateau borders radius as a function of the film thickness h obtained by SANS data analysis. Two regimes (1 and 2) are also represented and correspond to two drainage process as explained in section 5.

However, to better correlate their variation, thin film pressure balance measurements would be required[70]. Nevertheless if we analyse the variation of the Plateau border radius as a function of time via the image analysis (Fig. 7) and if we correlate this variation with those of the film thickness h (Fig. 10) we can determine two temporal phases as well. During the "fast phase" (end of phase 1 as shown in Fig. 10) the drainage and the induced film sucking by this hydrodynamic mechanism thins the film. This phase is too fast in comparison to the diffusion of the surfactant to relax the stress involved on the interfaces; the disjoining pressure increases without film thickness variation. Then in phase 2, once the drainage slows down, the system can relax and the film thins until an equilibrium thickness; hence an equilibrium pressure is reached. It is interesting to notice that the thinning velocity is close to zero (slope of the thickness variation versus time, see Fig. 9) when the contribution of the films to the foam specific surface area becomes larger than that of the Plateau borders. Both the liquid content of the foam and the Plateau border specific area show a similar bi-exponential decay supporting the idea that the drainage of the solution takes place

mainly through the Plateau borders [71,72]. After this transient period the foam aging enter in a self-similar growth regime where the mean radius of bubble $\langle r \rangle$ evolves in $t^{1/2}$.

6 Conclusion

In summary, the analysis of foam stability requires the collection of a wide range of information from the nano- to the centimetre scale that has to be correlated for a better understanding of the underlying processes. While such a multi-scale analysis is mostly performed using different techniques separately in the literature [36,39], herein the evolution of a foam has been followed simultaneously using macro-photography, electrical conductivity, and small-angle neutron scattering. The combination of these three techniques allows to perform this multiscale analysis in real time on a given sample. In particular, the analysis in absolute scale of the SANS data allows to quantify the specific surface areas from Plateau borders and from inter-bubble thin films as well for which time their evolution can be correlated to the film thickness variation, while the analysis of the SANS data in arbitrary units only provided reliable values for the foam film thickness [48,49].

To demonstrate the relevance of the method and the setup, the aging of a liquid foam stabilized by a non-ionic BrijO10 and anionic SDS surfactant mixture was studied. With this new device, we have been able to follow the evolution of the number of bubbles, liquid fraction by means of three different methods, but also the thickness of the inter-bubble film as well as the specific surface of the foam. To the best of our knowledge, it is the first report of the structural characterization of a liquid foam which simultaneously covers six orders of magnitude in size, from the nanometer scale of the micelles to the millimeter scale of the foam bubbles. From the evolution of the parameters, it was found that the aging of the foam follows a bi-exponential decay. An initial fast drying of the foam is due to the free drainage of the liquid through the Plateau borders. This process takes approximately 5-7 minutes to be completed. The free drainage is followed by further drying of the foam, where the liquid drainage is slowed down by capillary forces and repulsion between the foam films. This second drainage phase takes one hour approximately to be completed and to observe a self-similar regime of bubble growth. A rapid collapse of the foam follows its full drying once a critical disjoining pressure is achieved, about 1330 Pa for the studied system. This is the first time that a relationship between the disjunction pressure Π_d in foams under free drainage (so in out-of-equilibrium conditions) and the foam film thickness h has been measured. These experiments are generally done on single films in a thin-film pressure balance. Moreover, the final disjunction pressure values obtained are relatively low compared to the maximum value of disjunction pressure measured at rupture for the film alone [69] suggesting that the destabilization of the foam does not depend directly on disjunction pressure.

Getting such a detailed overview of the evolution of a foam is a fundamental step to tailor the foam for specific needs. For instance, one of the strategies to obtain wet foams is to reduce the drainage by adding thickeners [73]. The present approach allows to relate the characteristic times of drained with the thickener concentration, thus allowing for fine tuning the properties of the foam. In more general terms, having access to the details of the destabilization mechanisms of liquid foams is the prerequisite for designing novel foams with the desired properties.

Author Contributions

L.C., O.D. and J-L.B. conceived the project. L.C. and O.D. supervised the project, J.L., L.C., O.D. and P.B. conducted the experiments. J.L. participated in the development of the device. J.L., B.D., and L.C. performed data analysis. J.L., L.C. and O.D. discussed the results. All authors commented on the work and reviewed the manuscript.

Conflicts of interest

The authors declare that they have no competing interests.

References

[1] Chao Wang and Huazhou Andy Li. Stability and mobility of foam generated by gas-solvent/surfactant mixtures under reservoir conditions. *Journal of Natural Gas Science and Engineering*, 34:366–375, 2016.

[2] Masoud Hatami Alooghareh, Atefeh Kabipour, Mohamadhosein ghazavi, Seyyed Mohammad Mousavi Sisakht, and Mehdi Razavifar. Effects of different gases on the performance of foams stabilized by cocamidopropyl betaine surfactant and silica nanoparticles: A comparative experimental study. *Petroleum*, 2021.

[3] Su Nee Tan, Daniel Fornasiero, Rossen Sedev, and John Ralston. The role of surfactant structure on foam behaviour. *Colloids and Surfaces A: Physicochemical and Engineering Aspects*, 263(1):233–238, 2005.

[4] Z. Briceño-Ahumada and D. Langevin. On the influence of surfactant on the coarsening of aqueous foams. *Advances in colloid and interface science*, 244:124–131, 2017.

[5] Anne-Laure Biance, Aline Delbos, and Olivier Pitois. How topological rearrangements and liquid fraction control liquid foam stability. *Phys. Rev. Lett.*, 106:068301, 2011.

[6] Anniina Salonen, Romain Lhermerout, Emmanuelle Rio, Dominique Langevin, and Arnaud Saint-Jalmes. Dual gas and oil dispersions in water: production and stability of foamulsion. *Soft Matter*, 8:699–706, 2012.

[7] Eri Yoshida, Rouhollah Farajzadeh, Sebastian Vincent-Bonnieu, and Nacera Bourada Bourada. Effect of gas permeability and solubility on foam. *Journal of Soft Matter*, 2014:145352, 2014.

[8] Arnaud Saint-Jalmes. Physical chemistry in foam drainage and coarsening. *Soft Matter*, 2:836–849, 2006.

[9] Julia Boos, Wiebke Drenckhan, and Cosima Stubenrauch. Protocol for studying aqueous foams stabilized by surfactant mixtures. *Journal of Surfactants and Detergents*, 16(1):1–12, 2013.

[10] Vassili V. Yaminsky, Satomi Ohnishi, Erwin A. Vogler, and Roger G. Horn. Stability of aqueous films between bubbles. part 1. the effect of speed on bubble coalescence in purified water and simple electrolyte solutions. *Langmuir*, 26(11):8061–8074, 2010. PMID: 20146434.

[11] C. T. Nguyen, H. M. Gonnermann, Y. Chen, C. Huber, A. A. Maiorano, A. Gouldstone, and J. Dufek. Film drainage and the lifetime of bubbles. *Geochemistry, Geophysics, Geosystems*, 14(9):3616–3631, 2013.

[12] Jonas Miguet, Florence Rouyer, and Emmanuelle Rio. The life of a surface bubble. *Molecules*, 26(5), 2021.

[13] O. Arciniega Saavedra and J. Gracia Fadrique. Surface tension and foam stability prediction of polydimethylsiloxane-polyol systems. *Open Journal of Physical Chemistry*, 2(4):189–194, 2012.

[14] Krastanka G. Marinova, Elka S. Basheva, Boriana Nenova, Mila Temelska, Amir Y. Mirarefi, Bruce Campbell, and Ivan B. Ivanov. Physico-chemical factors controlling the foamability and foam stability of milk proteins: Sodium caseinate and whey protein concentrates. *Food Hydrocolloids*, 23(7):1864–1876, 2009.

[15] Daniela Georgieva, Alain Cagna, and Dominique Langevin. Link between surface elasticity and foam stability. *Soft Matter*, 5:2063–2071, 2009.

[16] K. Małysa, R. Miller, and K. Lunkenheimer. Relationship between foam stability and surface elasticity forces: Fatty acid solutions. *Colloids and Surfaces*, 53(1):47–62, 1991.

[17] E. S. Benilov, C. P. Cummins, and W. T. Lee. Why do bubbles in guinness sink? *American Journal of Physics*, 81(2):88–91, 2013.

[18] Gérard Liger-Belair and Clara Cilindre. How many co2 bubbles in a glass of beer? *ACS Omega*, 6(14):9672–9679, 2021. PMID: 33869947.

[19] William S. Y. Wong, Abhinav Naga, Lukas Hauer, Philipp Baumli, Hoimar Bauer, Katharina I. Hegner, Maria D'Acunzi, Anke Kaltbeitzel, Hans-Jürgen Butt, and Doris Vollmer. Super liquid repellent surfaces for anti-foaming and froth management. *Nature Communications*, 12(1):5358, 2021.

[20] Christopher Hill and Julian Eastoe. Foams: From nature to industry. *Advances in Colloid and Interface Science*, 247:496–513, 2017.

[21] Cyril Micheau, Dmytro Dedovets, Pierre Bauduin, Olivier Diat, and Luc Girard. Nanoparticle foam flotation for caesium decontamination using a ph-sensitive surfactant. *Environ. Sci.: Nano*, 6:1576–1584, 2019.

[22] Brent S. Murray. Recent developments in food foams. *Current Opinion in Colloid and Interface Science*, 50:101394, 2020.

[23] Florence Elias, Jérôme Crassous, Caroline Derec, Benjamin Dollet, Wiebke Drenckhan, Cyprien Gay, Valentin Leroy, Camille Noûs, Juliette Pierre, and Arnaud Saint-Jalmes. The acoustics of liquid foams. *Current Opinion in Colloid and Interface Science*, 50:101391, 2020.

[24] Talha Majeed, Muhammad Shahzad Kamal, Xianmin Zhou, and Theis Solling. A review on foam stabilizers for enhanced oil recovery. *Energy Fuels*, 35(7):101391, 2021.

[25] Pierre Trinh, Alesya Mikhailovskaya, Mengxue Zhang, Patrick Perrin, Nadège Pantoustier, Grégory Lefèvre, and Cécile Monteux. Leaching foams for copper and silver dissolution: A proof of concept of a more environmentally friendly process for the recovery of critical metals. *ACS Sustainable Chemistry & Engineering*, 9(42):14022–14028, 2021.

[26] Rakowska, Joanna. Best practices for selection and application of firefighting foam. *MATEC Web Conf.*, 247:00014, 2018.

[27] Tamara Schad, Natalie Preisig, Dirk Blunk, Heinrich Piening, Wiebke Drenckhan, and Cosima Stubenrauch. Less is more: Unstable foams clean better than stable foams. *Journal of Colloid and Interface Science*, 590:311–320, 2021.

[28] Cosima Stubenrauch, Martin Hamann, Natalie Preisig, Vinay Chauhan, and Romain Bordes. On how hydrogen bonds affect foam stability. *Advances in Colloid and Interface Science*, 247:435–443, 2017. Dominique Langevin Festschrift: Four Decades Opening Gates in Colloid and Interface Science.

[29] Reinhard Höhler, Sylvie Cohen-Addad, and Douglas J. Durian. Multiple light scattering as a probe of foams and emulsions. *Current Opinion in Colloid and Interface Science*, 19(3):242–252, 2014.

[30] Benjamin Dollet and Christophe Raufaste. Rheology of aqueous foams. *Comptes Rendus Physique*, 15(8):731–747, 2014. Liquid and solid foams / Mousses liquides et solides.

[31] D Langevin. Influence of interfacial rheology on foam and emulsion properties. *Advances in Colloid and Interface Science*, 88(1):209–222, 2000. Beijing Conference, May 1999.

[32] Stephan A. Koehler, Sascha Hilgenfeldt, and Howard A. Stone. A generalized view of foam drainage: Experiment and theory. *Langmuir*, 16(15):6327–6341, 2000.

[33] Arnaud Saint-Jalmes. Physical chemistry in foam drainage and coarsening. *Soft Matter*, 2:836–849, 2006.

[34] Anne-Laure Fameau, Arnaud Saint-Jalmes, Fabrice Cousin, Bérénice Houinsou Houssou, Bruno Novales, Laurence Navailles, Frédéric Nallet, Cédric Gaillard, François Boué, and Jean-Paul Douliez. Smart foams: Switching reversibly between ultrastable and unstable foams. *Angewandte Chemie International Edition*, 50(36):8264–8269, 2011.

[35] D. Varade, D. Carriere, L. R. Arriaga, A.-L. Fameau, E. Rio, D. Langevin, and W. Drenckhan. On the origin of the stability of foams made from catanionic surfactant mixtures. *Soft Matter*, 7:6557–6570, 2011.

[36] Isabelle Cantat, Cohen-Addad Sylvie, Elias Florence, Graner François, Hoehler Reinhard, Olivier Pitois, Rouyer Florence, and Arnaud Saint-Jalmes. *Foams: Structure and Dynamics*. Oxford University Press, 2013.

[37] Sébastien Andrieux, Pierre Muller, Manish Kaushal, Nadia Sofía Macias Vera, Robin Bollache, Clément Honorez, Alain Cagna, and Wiebke Drenckhan. Microfluidic thin film pressure balance for the study of complex thin films. *Lab Chip*, 21:412–420, 2021.

[38] Emmanouil Chatzigiannakis, Peter Veenstra, Dick ten Bosch, and Jan Vermant. Mimicking coalescence using a pressure-controlled dynamic thin film balance. *Soft Matter*, 16:9410–9422, 2020.

[39] Chrystian Ochoa, Shang Gao, Samanvaya Srivastava, and Vivek Sharma. Foam film stratification studies probe intermicellar interactions. *Proceedings of the National Academy of Sciences*, 118(25):8915–8924, 2021.

[40] Omar T. Mansour, Beatrice Cattoz, Manon Beaube, Morganne Montagnon, Richard K. Heenan, Ralf Schweins, Marie-Sousai Appavou, and Peter C. Griffiths. Assembly of small molecule surfactants at highly dynamic air–water interfaces. *Soft Matter*, 13:8807–8815, 2017.

[41] Shiho Yada, Hiroshi Shimosegawa, Hiroya Fujita, Munehiro Yamada, Yukako Matsue, and Tomokazu Yoshimura. Microstructural characterization of foam formed by a hydroxy group-containing amino acid surfactant using small-angle neutron scattering. *Langmuir*, 36(27):7808–7813, 2020.

[42] Raphaël Poryles, Thibaud Chevalier, Nicolas Gland, Elisabeth Rosenberg, and Loïc Barré. Characterization of foam flowing in a granular medium in the presence of oil by small angle neutron scattering. *Soft Matter*, 16:1771–1778, 2020.

[43] Cyril Micheau, Pierre Bauduin, Olivier Diat, and Sylvain Faure. Specific salt and ph effects on foam film of a ph sensitive surfactant. *Langmuir*, 29(27):8472–8481, 2013. PMID: 23758636.

[44] Li Zhang, Alesya Mikhailovskaya, Pavel Yazhgur, François Muller, Fabrice Cousin, Dominique Langevin, Nan Wang, and Anniina Salonen. Precipitating sodium dodecyl sulfate to create ultrastable and stimulable foams. *Angewandte Chemie International Edition*, 54(33):9533–9536, 2015.

[45] Jamie Hurcom, Alison Paul, Richard K. Heenan, Alun Davies, Nicholas Woodman, Ralf Schweins, and Peter C. Griffiths. The interfacial structure of polymeric surfactant stabilised air-in-water foams. *Soft Matter*, 10:3003–3008, 2014.

[46] I. Schmidt, B. Novales, F. Boué, and M.A.V. Axelos. Foaming properties of protein/pectin electrostatic complexes and foam structure at nanoscale. *Journal of Colloid and Interface Science*, 345(2):316–324, 2010.

[47] Stefania Perticaroli, Jana Herzberger, Yiping Sun, Jonathan D. Nickels, Ryan P. Murphy, Katie Weigandt, and Paula J. Ray. Multiscale microstructure, composition, and stability of surfactant/polymer foams. *Langmuir*, 36(48):14763–14771, 2020. PMID: 33232158.

[48] Max Hohenschutz, Isabelle Grillo, Charles Dewhurst, Philipp Schmid, Luc Girard, Alban Jonchère, Olivier Diat, and Pierre Bauduin. Superchaotropic nano-ions as foam stabilizers. *Journal of Colloid and Interface Science*, 603:141–147, 2021.

[49] Matthias Kühnhammer, Larissa Braun, Michael Ludwig, Olaf Soltwedel, Leonardo Chiappisi, and Regine von Klitzing. A new model to describe small-angle neutron scattering from foams. *Journal of Applied Crystallography*, 55(4):758–768, 2022.

[50] Monique A. V. Axelos and François Boué. Foams as viewed by small-angle neutron scattering. *Langmuir*, 19(17):6598–6604, 2003.

[51] Tobias Widmann, Lucas P. Kreuzer, Matthias Kühnhammer, Andreas J. Schmid, Lars Wiehemeier, Sebastian Jaksch, Henrich Frielinghaus, Oliver Löhmann, Harald Schneider, Arno Hiess, Regine von Klitzing, Thomas Hellweg, and Peter Müller-Buschbaum. Flexible sample environment for the investigation of soft matter at the european spallation source: Part ii—the gisans setup. *Applied Sciences*, 11(9), 2021.

[52] Feng Liu, Zhongni Wang, Dezhi Sun, Xilian Wei, Wu Zhou, Ganzuo Li, and Gaoyong Zhang. Adsorption kinetics of brij 97 at the air/solution interface. *Journal of Dispersion Science and Technology*, 27(5):657–663, 2006.

[53] Surajit Mukherjee and H. Wiedersich. Morphological and viscoelastic properties of dense foams generated from skin cleansing bars. *Colloids and Surfaces A: Physicochemical and Engineering Aspects*, 95:159–172, 1995.

[54] C. D. Dewhurst, I. Grillo, D. Honecker, M. Bonnaud, M. Jacques, C. Amrouni, A. Perillo-Marcone, G. Manzin, and R. Cubitt. The small-angle neutron scattering instrument D33 at the Institut Laue–Langevin. *Journal of Applied Crystallography*, 49(1):1–14, 2016.

[55] ILL. Grasp. https://www.ill.eu/users/support-labs-infrastructure/software-scientific-tools/grasp. [Online; accessed 22-July-2022].

[56] G. Bradski. The OpenCV Library. *Dr. Dobb's Journal of Software Tools*, 2000.

[57] Yingjie Wang and Stephen J. Neethling. The relationship between the surface and internal structure of dry foam. *Colloids and Surfaces A: Physicochemical and Engineering Aspects*, 339(1-3):73–81, 2009.

[58] Emilie Forel, Emmanuelle Rio, Maxime Schneider, Sebastien Beguin, Denis Weaire, Stefan Hutzler, and Wiebke Drenckhan. The surface tells it all: relationship between volume and surface fraction of liquid dispersions. *Soft Matter*, 12:8025–8029, 2016.

[59] K Feitosa, S Marze, A Saint-Jalmes, and D J Durian. Electrical conductivity of dispersions: from dry foams to dilute suspensions. *Journal of Physics: Condensed Matter*, 17(41):6301–6305, 2005.

[60] NIST. Neutron activation and scattering calculator. `https://www.ncnr.nist.gov/resources/activation`. [Online; accessed 22-July-2022].

[61] G. Porod. General theory. In O Glatter and O Kratky, editors, *Small angle x-ray scattering*, pages 17–51. New York : Academic Press, 1982.

[62] Wiebke Drenckhan and Stefan Hutzler. Structure and energy of liquid foams. *Advances in Colloid and Interface Science*, 224:1–16, 2015.

[63] Jan Skov Pedersen. Modelling of Small-Angle Scattering Data from Colloids and Polymer Systems. In Peter Lindner and Thomas Zemb, editors, *Neutrons , X-rays and Light : Scattering Methods Applied to Soft Condensed Matter*, pages 391–420. Elsevier Science Bv, 2002.

[64] Max Born. Quantenmechanik der Stoßvorgänge. *Zeitschrift für Physik*, 38(11):803–827, 1926.

[65] Alesya Mikhailovskaya, Li Zhang, Fabrice Cousin, François Boué, Pavel Yazhgur, François Muller, Cyprien Gay, and Anniina Salonen. Probing foam with neutrons. *Advances in Colloid and Interface Science*, 247:444–453, 2017. Dominique Langevin Festschrift: Four Decades Opening Gates in Colloid and Interface Science.

[66] Jeffrey Penfold and Robert K. Thomas. Neutron reflectivity and small angle neutron scattering: An introduction and perspective on recent progress. *Current Opinion in Colloid & Interface Science*, 19(3):198–206, 2014.

[67] Janine Etrillard, Monique A. V. Axelos, Isabelle Cantat, Franck Artzner, Anne Renault, Thomas Weiss, Renaud Delannay, and François Boué. In situ investigations on organic foam films using neutron and synchrotron radiation. *Langmuir*, 21(6):2229–2234, 2005.

[68] B. S. Gardiner, B. Z. Dlugogorski, and G. J. Jameson. Coarsening of two- and three-dimensional wet polydisperse foams. *Philosophical Magazine A*, 80(4):981–1000, 2000.

[69] Natascha Schelero, Gabi Hedicke, Per Linse, and Regine von Klitzing. Effects of counterions and co-ions on foam films stabilized by anionic dodecyl sulfate. *The Journal of Physical Chemistry B*, 114(47):15523–15529, 2010.

[70] Alesya Mikhailovskaya, Emmanouil Chatzigiannakis, Damian Renggli, Jan Vermant, and Cécile Monteux. From individual liquid films to macroscopic foam dynamics: A comparison between polymers and a nonionic surfactant. *Langmuir*, 38(35):10768–10780, 2022.

[71] Ralph A. Leonard and Robert Lemlich. A study of interstitial liquid flow in foam. part i. theoretical model and application to foam fractionation. *AIChE Journal*, 11(1):18–25, 1965.

[72] O. Pitois, E. Lorenceau, N. Louvet, and F. Rouyer. Specific surface area model for foam permeability. *Langmuir*, 25(1):97–100, 01 2009.

[73] Hetang Wang, Xiaobin Wei, Yunhe Du, and Deming Wang. Effect of water-soluble polymers on the performance of dust-suppression foams: Wettability, surface viscosity and stability. *Colloids and Surfaces A: Physicochemical and Engineering Aspects*, 568:92–98, 2019.